SEIS**MI**CA

Sparse fault representation based on moment tensor interpolation

Julien Thurin [iD] [* 1]

[1]Geophysical Institute and Department of Geosciences, University of Alaska Fairbanks, Fairbanks, Alaska, 99775

Abstract Accurate representation of large earthquake sources is required for understanding rupture dynamics and improving seismic hazard assessments. While capable of capturing complex spatio-temporal slip scenarios, traditional finite-fault models often suffer from over-parameterization, require strong regularization, and pose significant computational challenges, especially in rapid-response scenarios. Conversely, multiple point source (MPS) models reduce the rupture as a sequence of point sources but are inadequate to simulate short-period wavefield and static displacement. We introduce a hybrid source representation that leverages moment tensor interpolation to bridge the gap between these models. By treating moment tensors as "key" centroids of a tensor field, we construct geometrically coherent slip models that retain the spatial complexity of finite-fault models while maintaining MPS's computational efficiency and simplicity. Our method extends existing 2D tensor-field reconstruction techniques to moment tensors, allowing source-type-preserving interpolation and enabling sparse model approximation and source upscaling for numerical simulations. We demonstrate how our approach can benefit both the inverse and forward problems on the January 2024 Noto earthquake, computing a sparse approximation of the USGS NEIC source model with fewer than ten key tensors and computing full wavefield and static deformation from upscaled source distributions in a realistic 3D regional tomographic model using spectral-element method.

1 Introduction

Earthquake source characterization is a fundamental aspect of seismological studies and has played a major role in our understanding of rupture dynamics, Earth's structures, tectonics, and seismic hazards. For the vast majority of earthquakes, we can rely on a point-source approximation of the rupture process in the form of the seismic moment tensor (Dziewonski and Woodhouse, 1983), which represents the elastic response to a shear-dislocation on an infinitesimal fault plane. This point-source approximation has been extended to account for more complex source mechanisms, recognizing the limitations of simpler models in capturing the spatio-temporal complexity of large earthquake ruptures (typically M_w 7 and above), which are required to build a comprehensive understanding of large earthquakes and their associated hazards. Rapid and accurate estimation of the slip history for larger earthquakes has direct implications in crisis response, as it can directly inform ground-motion models (such as the U.S. Geological Survey's ShakeMaps, Worden et al., 2020), which in turn help inform emergency management and resource allocation immediately following a significant earthquake. Tsunami warning systems could also benefit from rapidly inferred slip models (Weinstein and Lundgren, 2008; Dutykh et al., 2013; Melgar and Bock, 2015; Lotto et al., 2019), especially in coastal areas near the event – even though most systems are currently relying on scaling laws and homogeneous slip models,

which yield satisfying prediction in the far field (An et al., 2018).

The most prevalent representation of large ruptures is the finite-fault model, where the rupture is assumed to occur on a predefined fault plane or a collection of planes, which are further subdivided into sub-faults. The slip on each sub-fault is then characterized through a slip inversion process commonly referred to as Finite-Fault Inversion (FFI), using a large extent of waveform data, alongside geodetic and tsunami observations when available (Delouis et al., 2002). For an overview of the Slip Inversion problem, readers may refer to Ide (2007). FFI is a notoriously ill-posed inverse problem that requires spatial and temporal regularization to achieve stability (Koch et al., 2019; Goldberg et al., 2022). This process also relies on hard-prior constraints, such as the fault plane location and dimensions, maximum slip on each sub-fault, and restrictions to the rake angle direction (Ji et al., 2002). Recent research efforts have pushed for more flexibility in fault parameterization, including varying dip angles (Ragon et al., 2018), deformed surfaces (Dutta et al., 2021; Wei et al., 2023), iterative fault trace refinement (Shimizu et al., 2019) or machine learning based approximation (Kheirdast et al., 2021). However, operational methods are still limited to simpler geometries due to computational constraints despite evidence suggesting that fault structures can significantly impact rupture dynamics. Furthermore, FFI is inherently a non-unique inverse problem (Razafindrakoto et al., 2015), making it an ideal candidate for uncertainty estimation (Beresnev, 2003),

*Corresponding author: jthurin@alaska.edu

such as Bayesian FFI (Minson et al., 2013) and trans-dimensional FFI (Dettmer et al., 2014). In practice, these approaches are often hindered by computational limitations and are not implemented in rapid-response products.

An alternative to the finite-fault representation is the decomposition of complex ruptures into a sequence of point sources (Kikuchi and Kanamori, 1982; Tsai et al., 2005; Yue and Lay, 2020; Jia et al., 2020a,b) known as the Multiple Point Sources (MPS) or Multiple Centroid Sources method. By leveraging the simplicity of individual centroid moment tensor inversion, this approach allows for rapid characterization of slip history using long-period W-phase seismic data. The number of centroids can be determined empirically by increasing the number of subevents until a specific statistical criterion, such as variance reduction, is achieved (Tsai et al., 2005). The simplicity of point sources inversion often enables the use of Bayesian methods for uncertainty estimate of the solution (Duputel et al., 2012; Duputel and Rivera, 2017; Shi et al., 2018; Kutschera et al., 2024).

The spatial distribution of these MPS is generally able to capture the underlying fault geometry, although prior constraints might be necessary to stabilize the inversion. Such constraints can be estimated using waveform back-propagation (Ren et al., 2022) or directly using the spatial extent of the aftershock distribution (Zhou et al., 2022; Kutschera et al., 2024). While finite fault models are often over-parameterized (with a large number of sub-faults not exhibiting any slip), MPS tend to under-parameterize the problem, resulting in a systematic underestimation of total moment (Yue and Lay, 2020). Another issue that stems from the compact nature of this representation is that it cannot be used directly to compute static displacement over large spatial extents, which limits the use of geodetic data in the inversion process.

In this study, we explore how the geometric properties of the moment tensor can be used to propose a hybrid parameterization that bridges the gap between finite-fault and multiple-point source (MPS) models. We aim to construct geometrically coherent models that capture the spatial complexity of large earthquake ruptures, similar to finite-fault models, while maintaining MPS models' computational efficiency and simplicity.

To do so, we turn to the field of tensor-field reconstruction and show that moment tensor interpolation allows for the seamless transition between any two distinct point sources. This provides a new basis for constructing fault parameterization based on interpolation, where the MPS become "key" tensors from which we can reconstruct a quasi-continuous tensor field. In the following, we give a brief recall on the moment tensor geometrical properties before detailing how 2×2 tensor interpolation introduced in (Hotz et al., 2010) can be extended to the 3×3 moment tensor using eigendecomposition. This methodology has strong ties with Kagan angular rotations (Kagan, 1991), and allows exploiting moment tensor geometrical properties to construct shortest-path rotations in the tensor space.

To demonstrate the practical uses of moment tensor interpolation, we propose two proof-of-concept applications:

1. sparse approximation of a pre-existing finite fault model: we show the potential for dimensionality reduction of this new source representation by approximating a finite-fault model for the January 1st, 2024 Noto earthquake, using only a few key tensors.

2. source upscaling: we show how moment tensor interpolation can be used to upscale an existing source model so that it can be used to compute accurate wavefield and static displacement using a spectral-element numerical solver in a 3D Earth model

Through these applications, we ought to demonstrate the interest of moment tensor interpolation in building hybrid source representation that benefits the inverse problem by promoting sparsity and the forward problem by allowing a quasi-continuous representation of a heterogeneous slip model based on a purely geometrical approach.

2 The seismic moment tensor

The seismic moment tensor $\mathbf{M}$ is a mathematical representation of small-to-moderate earthquake source processes (Dziewonski and Woodhouse, 1983; Aki and Richards, 2002). Under the point-source approximation, it encodes information relative to the source's geometry, type (regular faulting, crack opening, collapse, explosion), as well as its scalar moment. Formally, $\mathbf{M}$ is a second-order symmetric tensor, represented as a 3×3 matrix:

$$\mathbf{M} = \begin{pmatrix} M_{11} & M_{12} & M_{12} \\ M_{21} & M_{22} & M_{23} \\ M_{31} & M_{32} & M_{32} \end{pmatrix}, \qquad (1)$$

where components M_{ij} (with $i, j = 1, 2, 3$) correspond to the nine force couples applied over a volume around the source location. Given the symmetric nature of the tensor, it is solely defined by six independent force couples $\mathbf{M} = [M_{11}, M_{22}, M_{33}, M_{12}, M_{13}, M_{23}]$, that together, are adequate to represent a wide variety of source behaviors.

One particularly useful decomposition of the moment tensor is given by its eigendecomposition:

$$\mathbf{M} = \mathbf{U}\boldsymbol{\Lambda}\mathbf{U}^T, \qquad (2)$$

where $\mathbf{U}$ is a matrix containing the orthogonal eigenvectors $[\mathbf{u_1}, \mathbf{u_2}, \mathbf{u_3}]$, defining the tensor eigenframe, and $\boldsymbol{\Lambda}$ is a diagonal matrix containing the tensor eigenvalue triple $(\lambda_1, \lambda_2, \lambda_3)$. This decomposition lets us express any moment tensor as a combination of its singular *orientation* and *source type*. In addition, the moment tensor is defined by its Frobenius norm

$$\|\mathbf{M}\| = \sqrt{\sum_i \lambda_i^2}, \qquad (3)$$

which defines the overall *magnitude* of the tensor, which, together with orientation and source type, define a moment tensor space (Tape and Tape, 2012).

Analogous to tensor shape in other fields (Schultz and Kindlmann, 2010; Hotz et al., 2010), the source type is invariant under rotation (a pure double-couple can represent a normal, reverse and strike-slip fault and remains a double couple). Recognizing that permutation of the eigenvalues is equivalent to rotation, the set of normalized, ordered eigenvalues ($\lambda_1 \geq \lambda_2 \geq \lambda_3$) define the non-redundant space describing all moment tensors.

From these geometric considerations stems a convenient representation of moment tensor source type on the eigenvalue lune (Tape and Tape, 2012), where the location on the lune (lune latitude and lune longitude) is controlled by the values of the eigenvalue triple. The distance between source-types is defined as the arc distance over the lune surface, which is a geodesic in moment tensor space.

Thus, we can see that traveling along the shortest path in the moment tensor space is a matter of rotations: Rotation of the eigenframe and rotation about the center of the unit sphere along the lune surface. From this, it appears natural to define moment tensor interpolation as computing the tensor values along the geodesic between tensors in the moment tensor space.

3 Moment tensor interpolation

The simplest approach to interpolate between any two tensors would be a direct linear interpolation of the tensor components such that for tensor $\mathbf{M}_a$ and $\mathbf{M}_b$, the interpolation point at $t \in [0, 1]$ is given by the following linear combination:

$$\mathbf{M}(t) = (1 - t) * \mathbf{M}_a + t * \mathbf{M}_b. \tag{4}$$

While this is a convenient and straightforward approach, Hotz et al. (2010) have shown that it is not shape-preserving and can lead to abrupt changes in the orientation of the interpolated 2D symmetric second-order tensors. For seismic moment tensors, this translates to a non-source-type-preserving interpolation. To illustrate, consider the interpolation between two double-couple tensors (satisfying $\lambda_1 = -\lambda_3$ and $\lambda_2 = 0$). Using direct linear interpolation, the intermediate tensors are not guaranteed to maintain their source type, as shown in Figure 1.
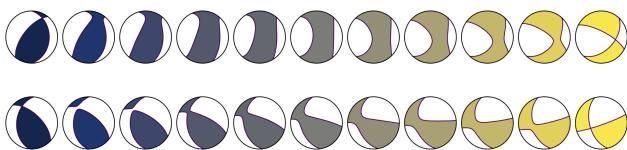
Figure 1 Interpolation between blue (t=0) and yellow (t=1) double-couple moment tensors picked at random, using the direct linear combination in equation 4. We see that this interpolation method is not source preserving and thus not along the geodesic path.

This problem arises because direct interpolation does not account for the geometric properties of the tensors, which causes the interpolation path to deviate from the geodesic path in moment tensor space. For pure double-couple sources, strike, dip, and rake angles offer a natural parameterization for describing focal mechanisms and can also serve as a basis for interpolation. When the fault plane is fixed, interpolating over rake angles alone provides a straightforward, source-preserving method. However, It has notable limitations, particularly when considering full moment tensor rotation: It may produce a sub-optimal interpolation path when angular distances are large or if differential rotation between all three angles is not scaled properly, leading to inconsistent rotational velocities. Thus, angular interpolation fails to generalize to cases where the fault plane is unknown or if non-double-couple components are present, requiring a more flexible approach capable of handling arbitrary source mechanisms.

To address this issue, we adopt a more natural approach to tensor interpolation, also described in Hotz et al. (2010), by treating eigenvalues and eigenvectors separately. Doing so, eigenvalues interpolation will solely be responsible for changes in source type (and therefore be represented by linear trajectories on the eigenvalue lune surface), while eigenvectors interpolation will only account for tensor orientation regardless of source type.

We thus define the interpolated moment tensor at $\mathbf{M}(t)$ with $t \in [0, 1]$ as

$$\mathbf{M}(t) = \mathbf{U}(t) \left[(1 - t)\mathbf{\Lambda}_a + t\mathbf{\Lambda}_b \right] \mathbf{U}(t)^T, \tag{5}$$

where $[(1 - t)\mathbf{\Lambda}_a + t\mathbf{\Lambda}_b]$ expresses the linear interpolation of the diagonal eigenvalues matrix containing the sorted eigenvalues of tensors $\mathbf{M}_a$ and $\mathbf{M}_b$, and $\mathbf{U}(t)$ is the interpolation of the eigenvector matrices. While the linear interpolation of eigenvalues is uniquely defined and simply operates on independent scalar values, it is not the case for $\mathbf{U}(t)$, which involves three-dimensional rotations. The complexity arises from the fact that 3D rotations are non uniquely defined (for each rotation by an angle θ around an Eulerian pole exists a counter-rotation about the same pole for $2\pi - \theta$ yielding the same result). There is also an ambiguity between eigenvector basis, as for an eigenvalue λ_i, both $\mathbf{u}_i$ and $-\mathbf{u}_i$ are valid eigenvectors, the choice of which might not guarantee the shortest rotation between two bases. Finally, in the presence of degenerate (or defective) eigenvalues (Golub and Van Loan, 1996), i.e., where two or more eigenvalues are equal, the eigenvectors associated with these eigenvalues span a subspace, leading to an infinity of valid orthonormal bases for that subspace. This makes finding the shortest rotation challenging as there are no unique shortest paths. To address some of these issues, we can implement the following strategies:

1. Aligning the eigenvectors: Before interpolation, we align the eigenvectors so that corresponding eigenvectors from the two tensors have the shortest angular distance. This can be done by generating all possible permutations of the interpolated tensors with respect to a "reference tensor," such that we can select the right-handed eigenvector-directions that minimize the rotational distance between equivalent eigenframes (amongst a set of 4

opposite-sign right-handed eigenvector combination). Right-handedness is defined as a positive determinant of the eigenvector matrix.

2. Use of quaternions and spherical-linear interpolation (Slerp): For interpolating the eigenvector matrices, we convert them into quaternions, which provide a robust mathematical framework for representing smooth rotations (Salamin, 1979). Using Slerp, we interpolate between the quaternions to ensure smooth and consistent rotations. Slerp addresses the non-linear nature of 3D rotations by interpolating along the shortest path on the 4D spherical hyper-surface of unit quaternions, thereby maintaining the orthogonality and continuity of the eigenvectors.

The issue of degenerate eigenvalues remains but should be marginal in practice, as degenerate tensors represent a negligible subset of the total moment tensor space (most notably at the edges of the eigenvalue lune).

The use of quaternions has been democratized in computer-generated graphics (Shoemake, 1985), together with spherical linear interpolation, where they are used to handle rigid body rotations in 3D space at a constant speed. They also eliminate potential risks associated with gimbal-locking which can otherwise cause a loss of rotational degrees of freedom when using Euler angles for rotations (Dam et al., 1998). A quaternion q is usually defined as the sum of a scalar q_0 and a vector $\mathbf{q} = (q_1, q_2, q_3)$ as

$$
\begin{aligned}
q &= q_0 + \mathbf{q} \\
&= q_0 + q_1\mathbf{i} + q_2\mathbf{j} + q_3\mathbf{k},
\end{aligned}
\tag{6}
$$

where $\mathbf{i}, \mathbf{j}, \mathbf{k}$ are the vectors defining a standard orthonormal basis. The quaternions used for rotations are typically *unit* quaternions, satisfying $q \cdot q = 1$ The relationship between the unit quaternion and a 3×3 orthogonal rotation matrix $\mathbf{U}$ is given by:

$$
\mathbf{U} = \begin{bmatrix} 1 - 2(q_2^2 + q_3^2) & 2(q_1q_2 - q_3q_0) & 2(q_1q_3 + q_2q_0) \\ 2(q_1q_2 + q_3q_0) & 1 - 2(q_1^2 + q_3^2) & 2(q_2q_3 - q_1q_0) \\ 2(q_1q_3 - q_2q_0) & 2(q_2q_3 + q_1q_0) & 1 - 2(q_1^2 + q_2^2) \end{bmatrix},
\tag{7}
$$

and conversely, the unit quaternion q is given by

$$
q = \pm \bar{q}/\|\bar{q}\|,
\tag{8}
$$

with

$$
\bar{q} = \begin{bmatrix} 1 + U_{11} - U_{22} - U_{33} \\ U_{12} + U_{21} \\ U_{13} + U_{31} \\ U_{23} - U_{32}. \end{bmatrix},
\tag{9}
$$

Note that there are three alternative expressions for $\bar{q}$ depending on the magnitude of elements in $\mathbf{U}$ (Markley, 2008).

From this, we can simply express the natural interpolation path between orientations by the Slerp between q_1 and q_2 (Shoemake, 1985)

$$
\begin{aligned}
q(t) &= \mathrm{Slerp}(q_a, q_b, t) \\
&= \frac{\sin((1-t)\theta)}{\sin(\theta)}q_a + \frac{\sin(t\theta)}{\sin(\theta)}q_b,
\end{aligned}
\tag{10}
$$

where θ is the angle between the quaternions q_a and q_b defined by $cos(\theta) = q_a \cdot q_b$, and where q_a and q_b are computed from $\mathbf{U}_a$ and $\mathbf{U}_b$ respectively and $|\cdot|$ expresses the dot product. $\mathbf{U}(t)$ is then given by applying equation 7 on $q(t)$.

Figure 2 shows the result of our interpolation scheme applied to the same pairs of tensors as in Figure 1. As the sorted eigenvalues are identical, the interpolation is achieved through the rotation of the eigenframe exclusively, and the source type is preserved through the whole transition from $t = 0$ to $t = 1$.
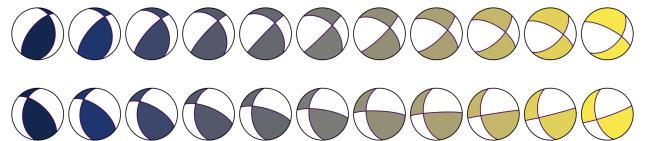
Figure 2 Interpolation between blue (t=0) and yellow (t=1) double-couple moment tensors used in Figure 1. By using the eigenvalue-eigenvector-based interpolation defined in equation 5, all intermediate tensors are double-couples. Interpolation occurs along the shortest rotation corresponding to the geodesic in tensor space.

In order to apply this scheme to three or more tensors, the eigenframe rotations are applied based on the sorted weights of each tensor, starting with the highest weight and proceeding in descending order. This prioritization ensures that the most influential key tensor (the one with the strongest weight) dictates the initial rotation, as 3D rotations are non-commutative and the order of application affects the outcome (except if the rotation axis is the same for all rotations). Trilinear interpolation based on direct linear combination and the corresponding tensor field using the proposed interpolation scheme are both shown in Figure 3. Using the direct linear interpolation method, we see that it fails at preserving the source type of all the interpolated tensors, whereas treating eigenvalues and eigenvectors separately allows for smooth rotation through the whole triangle.

Introducing a compensated linear vector dipole (CLVD) source as one of the three input tensors introduces degeneracy within the interpolated tensor field. This is apparent when using a simple linear combination, as illustrated in Figure 4. In contrast, when eigenvalues and eigenvectors are treated separately, the transition between source type and eigenframe occurs smoothly, without discontinuities (Figure 4). While double-couple tensors are typically used to characterize tectonic earthquake sources, constructing tensor fields that include non-double-couple sources may be valuable in other scenarios. For instance, in volcanic contexts, CLVD sources are commonly used to describe processes such as dyke intrusion or ring-faulting (Rodríguez-Cardozo et al., 2021).

Direct linear interpolation   Interpolation based on eigendecomposition
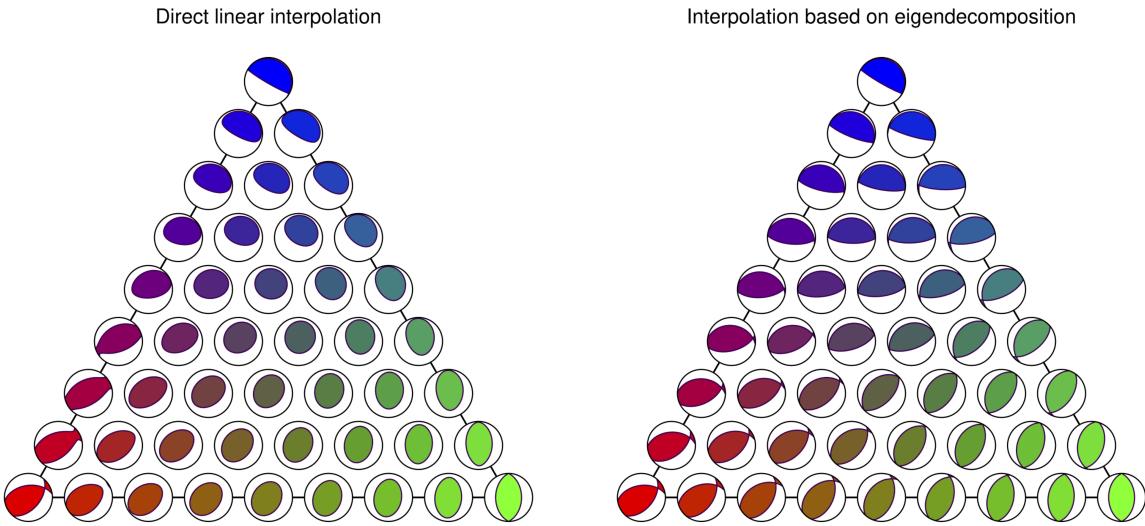
Figure 3 Trilinear tensor interpolation between three distinct double-couple tensors depicted in Red, Green, and Blue, located along the triangle vertices. (left) The interpolation follows equation 4. (right) This time, the interpolation follows equation 5, and source types are preserved within the interpolated tensor field. Color depicts weight along the RGB triangle values.

Direct linear interpolation   Interpolation based on eigendecomposition
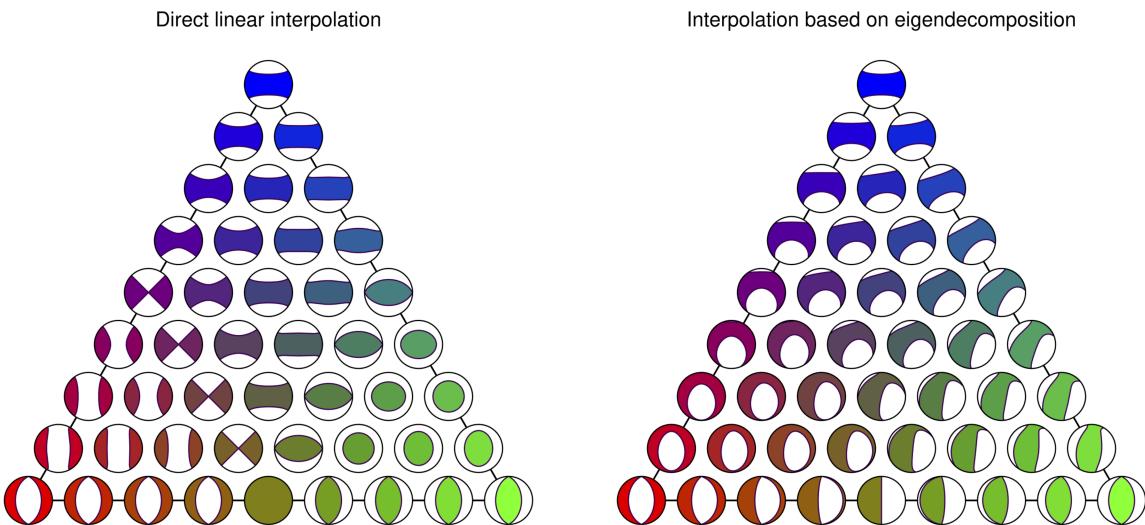
Figure 4 Trilinear tensor interpolation between two double-couples of opposite sign (Red and Green) and a compensated-linear-vector-dipole (Blue). (left) The interpolation follows equation 4 and cannot appropriately handle source-type interpolation smoothly. The eigenframes of the three tensors have been chosen so they share the same axes and create ambiguity. Consequently, the linear interpolation does not apply rotation due to the eigenframe ambiguity (all three sources share the same Cartesian basis). (right) The interpolation follows equation 5. The proposed interpolation scheme is able to maintain smooth rotations and source-type transitions (despite the Blue CLVD being a degenerate tensor). Color depicts weight along the RGB triangle values.

4 Application: sparse fault model and model upscaling

To illustrate the benefits of moment tensor interpolation in creating sparse representations of finite-fault models, we review the U.S. Geological Survey's (USGS) product for the January 1st, 2024, M_w 7.5 earthquake that struck the Noto peninsula, Japan. This earthquake occurred on an underwater fault system near Japan's western coast, resulting in significant damage, loss of life, and a significant tsunami in the Sea of Japan. In such scenarios, rapid slip estimation at depth could be valuable for effective tsunami early warning systems and post-event crisis response. It is thus desirable to obtain reliable, realistic slip models as fast as possible. One potential approach to achieve this is by reducing the number of free parameters considered in finite-fault inversions.

The USGS finite-fault products are part of the National Earthquake Information Center's (NEIC) routine operations and are estimated for significant earthquakes (typically $M_w \geq 7$, Hayes, 2017). From an initial Centroid Moment Tensor (CMT) estimate, a fault plane is chosen and divided into sub-fault patches on which the slip distribution is inverted using teleseismic P-wave data initially, and then integrating regional geodetic data when they become available (Goldberg et al., 2022). The USGS fault model for this event is composed of 315 sub-fault patches, spanning about 170 km along strike and 22 km along dip, based on a centroid moment tensor located at 37.5°N, 137.2°E and at a 10 km depth.

4.1 Sparse model approximation

We use the previously developed moment tensor interpolation method to approximate the existing tensor field from the NEIC, using 2D Gaussian mixtures such that the field is described as the sum of n 2D Gaussian functions, each acting as a support for a double-couple moment tensor, as illustrated with $n = 3$ in Figure 5. This approach allows us to represent the slip with a low number of "key" centroids, encoding the overall motion in this source model. Note that we are not inverting for a new slip distribution but demonstrating that a parsimonious parameterization of an existing model is feasible, and a dedicated inversion scheme compatible with this formalism will likely need to be evaluated before tackling direct slip inversion and is beyond the scope of this study.
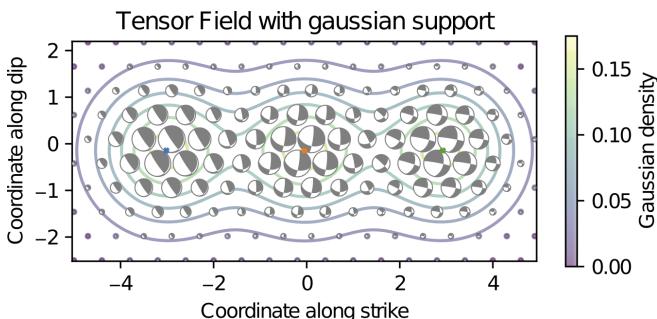
Figure 5 Tensor field computed from $n = 3$ key tensors, using unit covariance on a dummy fault plane. The blue, orange, and green crosses denote the location of the key tensors. The total probability density function is plotted as colored contours. Interpolated moment tensors at each grid point are shown in white and gray, with their sizes corresponding to relative magnitude. The Gaussian support controls both the moment density and the individual weight of each source during the interpolation.

Each Gaussian support is used as a weight for tensor combination, similar to inverse distance weighting in geospatial interpolation (Lu and Wong, 2008).

Given n key tensors located at positions $\mathbf{r}_i$ in the 2D fault plane with covariance matrix $\boldsymbol{\Sigma}_i$, the weight w_i for each position $\mathbf{r}$ in the original tensor field is given by the normalized Gaussian contribution:

$$w_i(\mathbf{r}) = \frac{e^{\left(-\frac{1}{2}(\mathbf{r}-\mathbf{r}_i)^T \boldsymbol{\Sigma}_i (\mathbf{r}-\mathbf{r}_i)\right)}}{\sum_{j=1}^{n} e^{\left(-\frac{1}{2}(\mathbf{r}-\mathbf{r}_j)^T \boldsymbol{\Sigma}_j (\mathbf{r}-\mathbf{r}_j)\right)}}. \quad (11)$$

Interpolating $\mathbf{M}(\mathbf{r})$ according to equation 5 allows us to express the weighted eigenvalue interpolation as

$$\boldsymbol{\Lambda}(\mathbf{r}) = \sum_{i=1}^{n} w_i(\mathbf{r}) \boldsymbol{\Lambda}_i, \quad (12)$$

where $\boldsymbol{\Lambda}_i$ are the eigenvalues of the i-th key moment tensor sorted by weights in descending order. The eigenframes $\mathbf{U}_i$ are converted to unit quaternions q_i. The quaternion interpolation is initialized by setting the unit quaternion associated with the highest weight q_1 such that

$$q_{\text{interp}} = q_1. \quad (13)$$

The successive weighted rotations are then applied according to

$$q_{\text{interp}} = \text{Slerp}(q_{\text{interp}}, q_i, w_i), \quad (14)$$

with $i = 2, ..., n$ before being converted back to the eigenvector matrix $\mathbf{U}(\mathbf{r})$ following equation 7. After computing both interpolated eigenvalues and eigenvectors, the interpolated moment tensor at $\mathbf{r}$ is expressed as

$$\mathbf{M}_{\text{interp}}(\mathbf{r}) = w(\mathbf{r})\mathbf{U}(\mathbf{r})\boldsymbol{\Lambda}(\mathbf{r})\mathbf{U}(\mathbf{r})^T, \quad (15)$$

where $w(\mathbf{r}) = \sum_{j=1}^{n} e^{\left(-\frac{1}{2}(\mathbf{r}-\mathbf{r}_j)^T \boldsymbol{\Sigma}_j (\mathbf{r}-\mathbf{r}_j)\right)}$ is the total Gaussian density at $\mathbf{r}$ that controls the magnitude of each interpolated tensor.

Finding the set of key tensors that best represent the original tensor field amounts to solving the following minimization problem:

$$\min_{\mathbf{r}_i, \boldsymbol{\Sigma}_i, \mathbf{M}_i} \mathcal{C} = \frac{\sum_{\mathbf{r} \in \mathcal{R}} \|\mathbf{M}_{\text{interp}}(\mathbf{r}) - \mathbf{M}_{\text{obs}}(\mathbf{r})\|^2}{\sum_{\mathbf{r} \in \mathcal{R}} \|\mathbf{M}_{\text{obs}}(\mathbf{r})\|^2}, \quad (16)$$

where $\mathbf{r}_i$, $\boldsymbol{\Sigma}_i$ and $\mathbf{M}_i$ are the positions, covariance matrices, and key moment tensors respectively for $i = 1, ..., n$, and $\mathcal{R}$ is the set of all positions in the fault plane where the USGS NEIC solution's tensors are located. The number of free parameters is thus $9 \times n$: 2 parameters for $\mathbf{r}_i$, 3 for $\boldsymbol{\Sigma}_i$, and 4 for $\mathbf{M}_i$ (magnitude, strike, dip, and rake). While the number of parameters could be slightly reduced by assuming the strike and dip angles known, we chose to keep these extra free parameters to demonstrate potential compatibility with the potency-density inversion method of Yamashita et al. (2022).

Working from the CMTSOLUTION file format available from the USGS NEIC model page, we approximate the 315 discrete point sources (converted from the original sub-fault used for the inversion) with $n = [1, ..., 9]$ centroids with their respective Gaussian support. In this example, the rupture velocity is kept fixed, though it could be estimated alongside the key tensors' locations in space. Finally, the fault plane is divided into n zones of equal area, to which each key tensor's location is assigned, preventing key tensors from overlapping.

The approximation is computed by black-box optimization of the n key tensors using the Covariance Matrix Adaptation Evolution Strategy (CMA-ES, Hansen and Ostermeier, 1996, 2001) python package pycma (Hansen et al., 2019) to minimize equation 16. Figure 6 shows the evolution of model fit with respect to
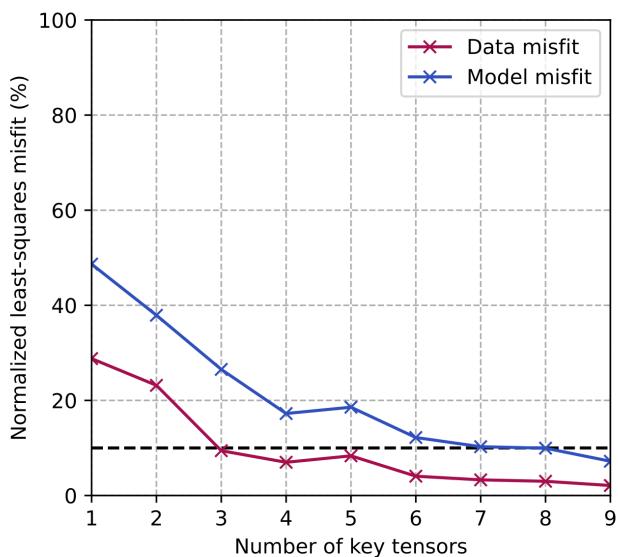
Figure 6 Normalized least-squares misfit for the set of $n = [1, ..., 9]$ key tensors. The blue curve represents the direct model fit in percentage. The red curve represents the normalized misfit between the static displacement computed in the original USGS NEIC model and the nine static displacement fields computed in SPECFEM3D Cartesian. The black-dashed line represents 10% of normalized misfit. Both misfit curves follow a similar trend, and the overall data misfit is lower than the model misfit, meaning sensible approximation can be achieved with very sparse models. The misfit increase from four to five key tensors might be explained by a sub-optimal spatial distribution of the key tensor sources or the stochastic nature of the optimization method.

the number of key tensors. We see that the approximation improves with the number of centroids and that more than 90% of the model can be explained with as few as eight key sources. Considering the USGS NEIC model is discretized over 315 sub-faults, the number of unknown parameters in the original model amounts to 1260 (for rake angle, rise time, rupture time, and moment"). By contrast, our approach reduces the number of free parameters to 81, using nine key tensors, each defined by nine parameters. While the temporal aspect has been left out for the sake of simplicity, adding the rupture time and rise time would raise the approximation to 99 parameters, which is still a significant improvement over the original parameterization. We also note that strike and dip angles could have been left out of the application to further reduce the number of unknowns. They have been kept as free parameters to demonstrate the potential for more general applications, particularly for scenarios where fault geometry is unknown or where tensors are projected onto non-planar parametric surfaces.

The USGS NEIC moment tensor field, along with the worst and best-interpolated tensor fields ($n = 1$ and 9 respectively), are shown in Figure 7. This demonstrates that smooth interpolation supported by simple basis functions can capture the main features of the original tensor field. This sparse source representation

takes advantage of the generally smooth nature of finite-fault models, which stems from the strong regularization they require for stability.

With these models at hand, we now turn to spectral element simulation to compute their associated displacement field in order to compare their performance in the data space.

4.2 Source upscaling for spectral element simulation

In order to compare the performance of our sparse source representations in the data space, it is necessary to upscale the inverted source models to ensure they are suitable for spectral element simulations. Upscaling helps evenly distribute the moment release over space and time, thus preventing artifacts from using large point sources in waveform simulations. Although these artifacts typically do not affect the wavefield's dynamic part, they can significantly impact the static displacement, especially for shallow sources. Previous application of source upscaling via interpolation has been presented in Tinti et al. (2005), in order to satisfy finite-difference stability criteria. In their approach, bicubic interpolation was used to smooth the slip distribution over an existing set of sub-faults, with the intent of preserving the rake angle of each sub-fault.

To achieve this from our point source representation, we adopt an iterative source upscaling approach based on the subdivision of a triangular mesh of point sources, as illustrated in Figure 8.

At each iteration, moment tensor interpolation is used to compute the barycenter of each triangle's edges (new moment tensor and location), along with its origin time, which is linearly interpolated. The moment of each seismic source is adjusted to accommodate the additional sources to preserve the original moment in the upscaled model. This source upscaling strategy effectively spreads moment release smoothly over space and time, helping to avoid artifacts associated with point sources in waveform simulation. While Tinti et al. (2005) interpolation scheme aimed at preserving the original rake angle of each subfault, we do not impose such a constraint in favor of a smooth transition both in moment and orientation of the additional sources. Applying four subdivisions of the original triangular mesh of $n = 315$ sources with an average source magnitude of Mw = 5.52, we end up with $n = 70311$ sources with an average source magnitude of Mw = 3.94, such that the original moment remains the same. Note that if required, the formulation in equation 5 can be extended to higher-order interpolation schemes for both moment and rotation control (Shoemake, 1985).

We then use our upscaled source models to produce full waveform simulations with the 3D spectral element method code SPECFEM3D Cartesian 4.1.0 (Komatitsch and Tromp, 2002a,b; Komatitsch et al., 2024). The simulation domain is based on the 3D regional Community Velocity Model for the Japanese Islands (Simutė et al., 2016; Fichtner et al., 2018), with topography resampled from ETOPO1 (Amante and Eakins, 2009). While we are primarily interested in the static vertical displacement
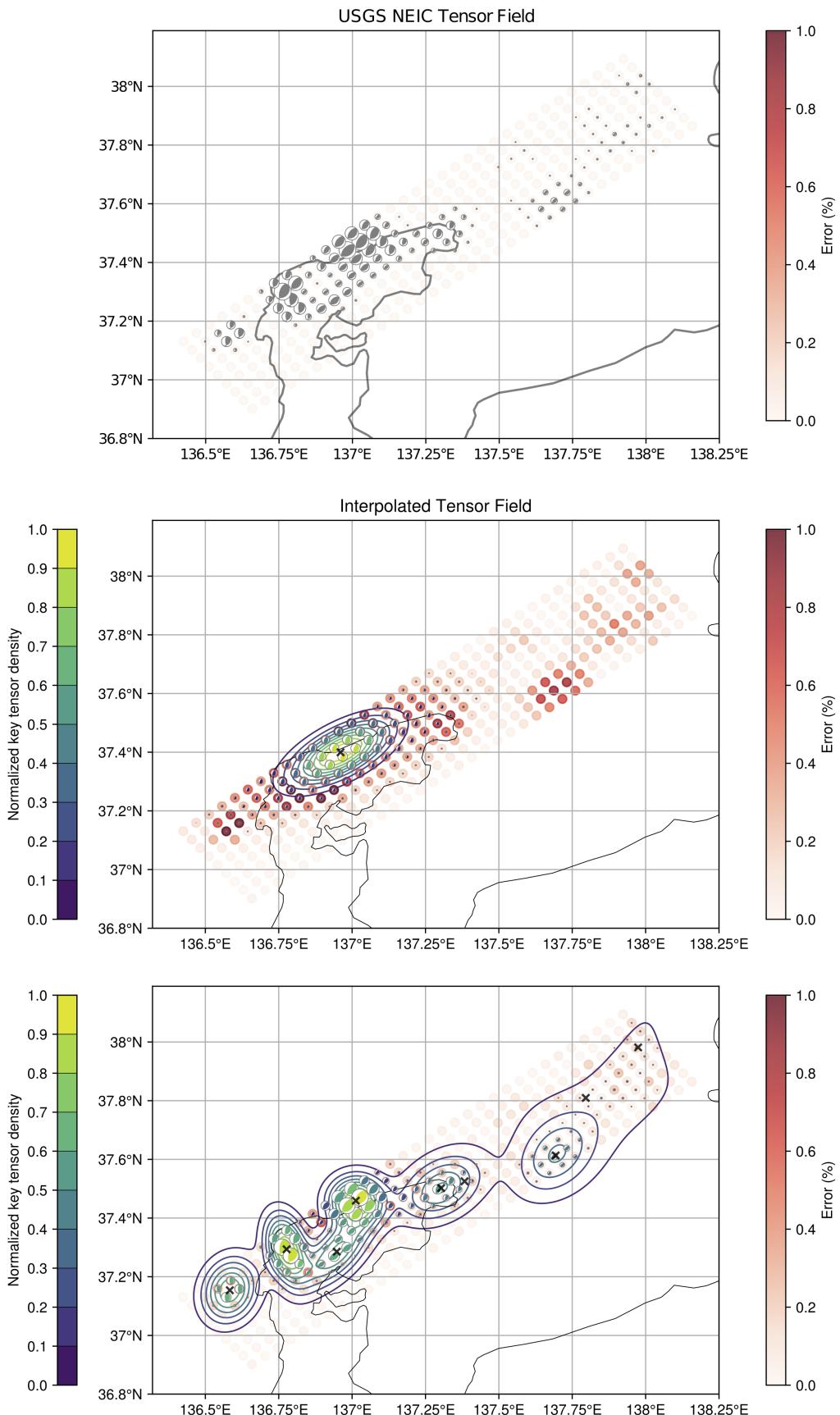
Figure 7 Moment tensor solution for (from top to bottom) the USGS NEIC model, the interpolated model with $n = 1$ key tensor, and the interpolated model with $n = 9$ tensors. Moment tensor sizes denote relative magnitude. Scattered colored points represent the source-wise normalized misfit in percentage, clipped at 1%. The total misfit with $n = 1$ is $\mathcal{C} \sim 48.7\%$. For $n = 9$, it goes down to $\mathcal{C} \sim 7.2\%$ total model error. Contour lines and Moment tensor colors represent the normalized sum of Gaussian densities, illustrative of the support of the interpolated field. Black crosses denotes position of the key tensors.

in this application, note that this allows computing the full wavefield with a period accuracy of about 2 seconds. The final vertical displacement fields from the original USGS model and its low-dimensional approximation with $n = 9$ key tensors are shown in Figure 9, demonstrating that their spatial features are comparable. We retrieve the three main displacement patches extending toward the Southwest end of the fault and the weak, diffuse uplift toward the Northeast end of the rupture. The absolute maximum difference is about 40 cm and the approximation is close (although not identical) to the original model. The normalized misfit curve between the USGS NEIC displacement and our 9 tensor-fields realizations is shown in Figure 6.

The fit in data space follows the same general trend as the model fit, decreasing with the number of sources. This result also re-emphasizes the non-uniqueness of the finite-fault inversion (FFI) problem, with fits in data space being significantly better than fits in the model space, showing that variability in the source model does not directly translate to variability in synthetic displacements. It also illustrates that despite the apparent complexity of the original model, a parsimonious parameterization could be used for the inversion without dramatic impact on the generated synthetic data.

5 Discussion

The applications presented in the previous section demonstrate that using moment tensor interpolation to represent ruptures provides significant advantages: It allows for dimensionality reduction of the inverse problem without compromising forward modeling capabilities.

In this context, it means we can simplify FFI by reducing the number of free parameters, leading to a better-posed inverse problem. With fewer parameters, the inversion process also becomes more computationally efficient, allowing for faster slip estimates and possibly incorporating uncertainty estimation methods in scenario-based tsunami warning systems. A promising avenue for future development is the application of a trans-dimensional Bayesian framework (Sambridge et al., 2006) to jointly estimate key-tensor parameters and determine the ideal number of key tensors, thus minimizing the risk of over-parameterization, which is a potential issue with the current NEIC solutions. Note that such framework has already been applied to FFI based on Voronoi tessellation of a pre-defined fault plane and sub-faults (Dettmer et al., 2014).

Using the concept of key moment tensors also opens up possibilities for jointly estimating both the geometry and the slip model. While we have made the choice of simplicity to present this parameterization and relied on a pre-existing 2D plane, this parameterization provides a solid basis for an extension to non-planar faults: each key centroid contains important information about geometry, encoded in the eigenframe of each tensor (and in turn, its fault planes). This can be leveraged to parameterize deformed 3D surfaces using splines (where the tensor eigenframes can be used as control points), allowing for dynamic location and in-

version for slip in a 3D space without relying on predefined fixed fault planes. The relevance of this tensor-based geometry estimation has been demonstrated by Shimizu et al. (2020), where fault geometry is updated a posteriori to the potency-density tensor-based inversion of the slip. This inversion process could become fully dynamic by alleviating computational constraints and enabling joint estimation of geometry and slip. Note that the current parameterization would readily allow consideration of multiple independent fixed fault planes without algorithmic modifications by distributing key tensors on these prescribed fault planes.

Several practical and exploratory questions remain to be answered to tackle slip inversion with this novel parameterization. One main question is how to handle the time evolution of the rupture. The origin time of each key tensor could be explicitly inverted, allowing us to invert for its strike, dip, and rake angles, location along the fault, and origin time. Alternatively, we could impose a fixed time interval between each key tensor and let their relative positions in space define the overall kinematics of the rupture. This approach would allow the apparent rupture velocity to be controlled by the spatial positions of the tensors. While this might require more key tensors to reconstruct complex rupture history, it eliminates potential tradeoffs between source location and origin time by explicitly encoding both in space-time coordinates.

Another key temporal aspect not assessed in our example application is how to tune the half duration of each source. As we work with increasingly numerous but also smaller sources via upscaling, the half-duration of each source should converge toward shot impulse functions (if the number of sources grows towards infinity to emulate a continuous rupture, their half-duration should diminish accordingly). However, due to numerical simulation constraints, working with extremely small half-durations may introduce unresolved high-frequency signals in the simulations. Careful analyses will need to be conducted to assess if source-upscaling can simulate the full wavefield without introducing artifacts from source duration. In our application, the source's half-durations were kept constant and determined internally by SPECFEM3D Cartesian, according to temporal resolution criteria.

Another major question is how to best alternate between the full 3D domain used in waveform simulation and the inverse problem, which lies on a 2D manifold (relative to coordinates on the fault). While projection between 3D and 2D spaces is trivial for a perfectly planar fault, it may require specific considerations for deformed surfaces or multiple independent fault planes. Techniques from the fields of dimensionality reduction and manifold learning may help in that regard (Ma and Fu, 2012; Ghojogh et al., 2023), but the optimal projection techniques and their efficient implementation in an inversion framework will require further investigation, particularly when multiple faults need to be considered.

Finally, in order to afford the use of 3D full-waveform modeling in a crisis-response scenario, we will have to take advantage of precomputed receiver-side Green's function in order to rapidly evaluate the Earth's re-
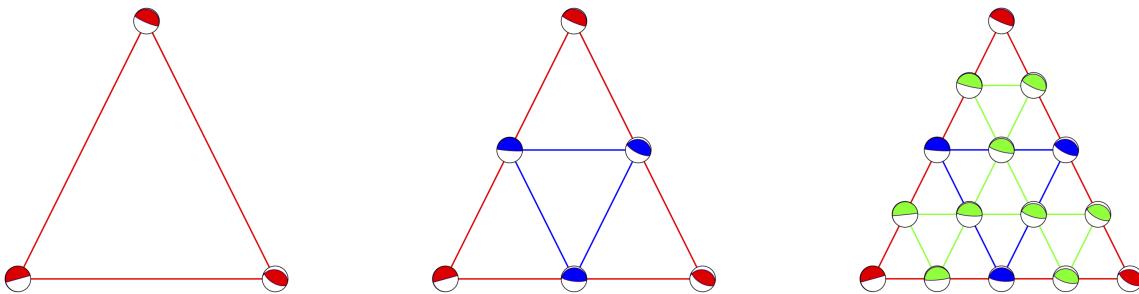
Figure 8 Iterative source upscaling on a single triangle. A two-step upscaling is shown here. Red tensors and triangles denote the original moment tensors. The results of the first and second iterations are shown in blue and green, respectively. All new tensors correspond to the interpolation scheme of equation 5 with $t = 0.5$. Iterations are shown sequentially from left to right, from (left) to (middle) and (middle) to (right).
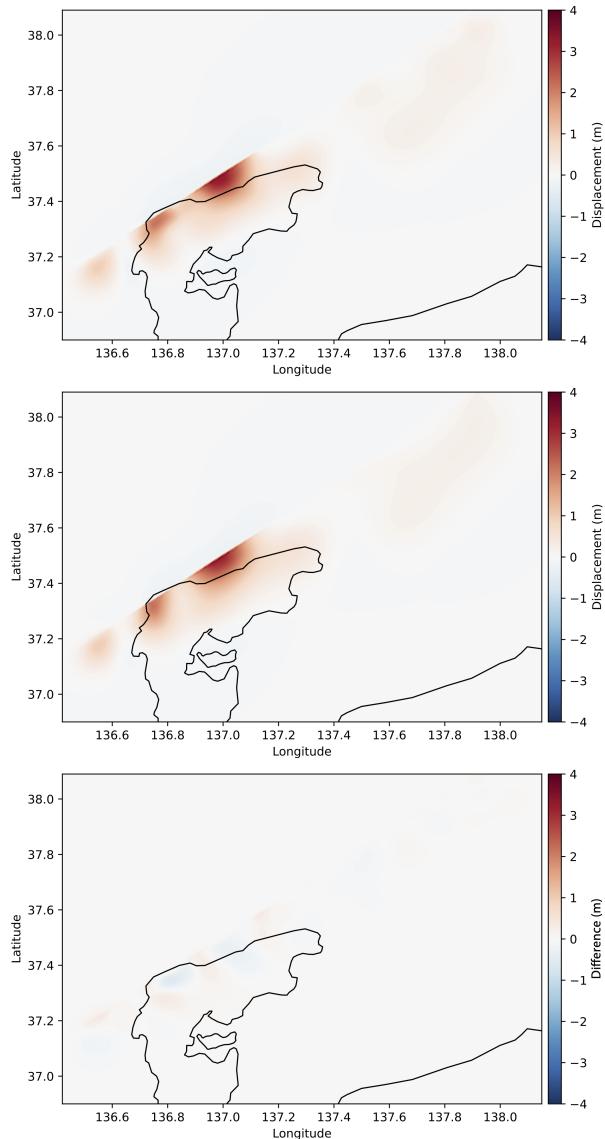
Figure 9 Static displacement maps are computed from the SPCEFEM3D Cartesian simulations using upscaled source models in a 3D regional model and topography. From top to bottom, upscaled USGS NEIC model, approximated model with $n = 9$ key tensors, and difference between the two maps.

sponse between any sources into a 3D volume and a set of pre-defined receiver locations. While it would be computationally challenging to do so systematically for the whole Earth, it should be possible to precompute databases of practical size for regions of interest, particularly for tsunamigenic areas along subduction zones or known large strike-slip systems. Inversion would otherwise have to be conducted from 1D Green's function databases (such as global Axisem databases provided by the Syngine data product, Nissen-Meyer et al., 2014; Krischer et al., 2017) at the cost of accuracy in locating sources in space.

6   Conclusion

This manuscript demonstrates a compact, efficient, and natural representation of quasi-continuous ruptures from moment tensor interpolant functions, which ought to fill the gap between FFI and MPS models. The interpolation method is sound regarding its geometrical implications, preserving source type and maintaining geodetic paths within the moment tensor space, ensuring consistent representation of rupture surfaces. It opens up new possibilities in terms of how we approach the FFI problem by lifting the dimensionality complexity, promoting sparsity, and, therefore, lowering the requirement for regularization. This approach also facilitates full wavefield simulations using spectral-elements numerical solvers. This was demonstrated by down-sizing the USGS NEIC source model for Japan's January 1st, 2024, Noto earthquake, using an approximation based on a few key tensors and recovering comparable surface displacements with an upscaled source model. The dimensionality reduction that this parameterization enables should open opportunities to tackle ambitious FFI problems, such as uncertainty quantification and joint geometry-slip characterization.

Acknowledgements

Data and code availability

The USGS NEIC model was obtained from https://earthquake.usgs.gov/product/finite-fault/ us6000m0xl_1/us/1704922177476/CMTSOLUTION (*last accessed July 2024*). Numerical modeling was conducted using SPECFEM3D_Cartesian available at https://github.com/SPECFEM/specfem3d. ETOPO1 elevation data in netcdf format used for simulation in SPECFEM3D was downloaded from https://www.ngdc.noaa.gov/mgg/global/relief/ETOPO1/ data/ice_surface/cell_registered/netcdf/(*last accessed June 2024*). The regional tomographic model used for simulation in SPECFEM3D was downloaded from the EarthScope Earth Model Collaboration https://ds.iris.edu/ds/products/emc-csem_japan/ (last accessed June 2024). The scripts including moment tensor interpolation routines to reproduce figure 3 to 5 are available on Zenodo at https://zenodo.org/records/13359347.

Competing interests

The author has no competing interests.

References

Aki, K. and Richards, P. G. *Quantitative seismology*. University Science Books, 2002.

Amante, C. and Eakins, B. ETOPO1 1 Arc-Minute Global Relief Model: Procedures, Data Sources and Analysis, 2009. NOAA Technical Memorandum NESDIS NGDC-24, National Geophysical Data Center, NOAA. doi:10.7289/V5C8276M, Accessed: June 2024.

An, C., Liu, H., Ren, Z., and Yuan, Y. Prediction of Tsunami Waves by Uniform Slip Models. *J. Geophys. Res. Oceans*, 123(11): 8366–8382, 2018. doi: https://doi.org/10.1029/2018JC014363.

Beresnev, I. A. Uncertainties in Finite-Fault Slip Inversions: To What Extent to Believe? (A Critical Review). *Bull. Seismol. Soc. Am.*, 93(6):2445–2458, 2003. doi: 10.1785/0120020225.

Dam, E., Koch, M., and Lillholm, M. Quaternions, interpolation and animation. WorkingPaper 5, Datalogisk Institut, Københavns Universitet, 1998.

Delouis, B., Giardini, D., Lundgren, P., and Salichon, J. Joint Inversion of InSAR, GPS, Teleseismic, and Strong-Motion Data for the Spatial and Temporal Distribution of Earthquake Slip: Application to the 1999 İzmit Mainshock. *Bull. Seismol. Soc. Am.*, 92(1): 278–299, 2002. doi: 10.1785/0120000806.

Dettmer, J., Benavente, R., Cummins, P. R., and Sambridge, M. Trans-dimensional finite-fault inversion. *Geophys. J. Int.*, 199(2): 735–751, 2014. doi: 10.1093/gji/ggu280.

Duputel, Z. and Rivera, L. Long-period analysis of the 2016 Kaikoura earthquake. *Phys. Earth Planet. Inter.*, 265:62–66, 2017. doi: https://doi.org/10.1016/j.pepi.2017.02.004.

Duputel, Z., Kanamori, H., Tsai, V. C., Rivera, L., Meng, L., Ampuero, J.-P., and Stock, J. M. The 2012 Sumatra great earthquake sequence. *Earth Planet. Sci. Lett.*, 351-352:247–257, 2012. doi: https://doi.org/10.1016/j.epsl.2012.07.017.

Dutta, R., Jónsson, S., and Vasyura-Bathke, H. Simultaneous Bayesian Estimation of Non-Planar Fault Geometry and Spatially-Variable Slip. *J. Geophys. Res. Solid Earth*, 126(7):e2020JB020441, 2021. doi: https://doi.org/10.1029/2020JB020441.

Dutykh, D., Mitsotakis, D., Gardeil, X., and Dias, F. On the use of the finite fault solution for tsunami generation problems. *Theor. Comput. Fluid Dyn.*, 27(1):177–199, 2013. doi: 10.1007/s00162-011-0252-8.

Dziewonski, A. M. and Woodhouse, J. H. An experiment in systematic study of global seismicity: Centroid-moment tensor solutions for 201 moderate and large earthquakes of 1981. *J. Geophys. Res. Solid Earth*, 88(B4):3247–3271, 1983. doi: https://doi.org/10.1029/JB088iB04p03247.

Fichtner, A., van Herwaarden, D.-P., Afanasiev, M., Simutė, S., Krischer, L., Çubuk Sabuncu, Y., Taymaz, T., Colli, L., Saygin, E., Villaseñor, A., Trampert, J., Cupillard, P., Bunge, H.-P., and Igel, H. The Collaborative Seismic Earth Model: Generation 1. *Geophys. Res. Lett.*, 45(9):4007–4016, 2018. doi: https://doi.org/10.1029/2018GL077338.

Ghojogh, B., Crowley, M., Karray, F., and Ghodsi, A. *Elements of dimensionality reduction and manifold learning*. Springer, 2023. doi: https://doi.org/10.1007/978-3-031-10602-6.

Goldberg, D. E., Koch, P., Melgar, D., Riquelme, S., and Yeck, W. L. Beyond the Teleseism: Introducing Regional Seismic and Geodetic Data into Routine USGS Finite-Fault Modeling. *Seismol. Res. Lett.*, 93(6):3308–3323, 2022. doi: 10.1785/0220220047.

Golub, G. H. and Van Loan, C. F. *Matrix computations (3rd ed.)*. Johns Hopkins University Press, USA, 1996.

Hansen, N. and Ostermeier, A. Adapting arbitrary normal mutation distributions in evolution strategies: the covariance matrix adaptation. In *Proceedings of IEEE International Conference on Evolutionary Computation*, pages 312–317, 1996. doi: 10.1109/ICEC.1996.542381.

Hansen, N. and Ostermeier, A. Completely Derandomized Self-Adaptation in Evolution Strategies. *Evolutionary Computation*, 9(2):159–195, 2001. doi: 10.1162/106365601750190398.

Hansen, N., Akimoto, Y., and Baudis, P. CMA-ES/pycma on Github. Zenodo, DOI:10.5281/zenodo.2559634, 2019. doi: 10.5281/zenodo.2559634.

Hayes, G. P. The finite, kinematic rupture properties of great-sized earthquakes since 1990. *Earth Planet. Sci. Lett.*, 468:94–100, 2017. doi: https://doi.org/10.1016/j.epsl.2017.04.003.

Hotz, I., Sreevalsan-Nair, J., Hagen, H., and Hamann, B. Tensor Field Reconstruction Based on Eigenvector and Eigenvalue Interpolation. In Hagen, H., editor, *Scientific Visualization: Adv. Concepts*, volume 1 of *Dagstuhl Follow-Ups*, pages 110–123. Schloss Dagstuhl – Leibniz-Zentrum für Informatik, Dagstuhl, Germany, 2010. doi: 10.4230/DFU.SciViz.2010.110.

Ide, S. Slip Inversion. In Schubert, G., editor, *Treatise on Geophysics*, pages 193–223. Elsevier, Amsterdam, 2007. doi: https://doi.org/10.1016/B978-044452748-6.00068-7.

Ji, C., Wald, D. J., and Helmberger, D. V. Source Description of the 1999 Hector Mine, California, Earthquake, Part I: Wavelet Domain Inversion Theory and Resolution Analysis. *Bull. Seismol. Soc. Am.*, 92(4):1192–1207, 2002. doi: 10.1785/0120000916.

Jia, Z., Shen, Z., Zhan, Z., Li, C., Peng, Z., and Gurnis, M. The 2018 Fiji Mw 8.2 and 7.9 deep earthquakes: One doublet in two slabs.

Earth and Planetary Science Letters, 531:115997, 2020a. doi: https://doi.org/10.1016/j.epsl.2019.115997.

Jia, Z., Wang, X., and Zhan, Z. Multifault Models of the 2019 Ridgecrest Sequence Highlight Complementary Slip and Fault Junction Instability. *Geophysical Research Letters*, 47(17):e2020GL089802, 2020b. doi: https://doi.org/10.1029/2020GL089802.

Kagan, Y. Y. 3-D rotation of double-couple earthquake sources. *Geophysical Journal International*, 106(3):709–716, 09 1991. doi: 10.1111/j.1365-246X.1991.tb06343.x.

Kheirdast, N., Ansari, A., and Custódio, S. Neuro-Fuzzy Kinematic Finite-Fault Inversion: 1. Methodology. *J. Geophys. Res. Solid Earth*, 126(8):e2020JB020770, 2021. doi: https://doi.org/10.1029/2020JB020770.

Kikuchi, M. and Kanamori, H. Inversion of complex body waves. *Bull. Seismol. Soc. Am.*, 72(2):491–506, 1982. doi: 10.1785/BSSA0720020491.

Koch, P., Bravo, F., Riquelme, S., and Crempien, J. G. F. Near-Real-Time Finite-Fault Inversions for Large Earthquakes in Chile Using Strong-Motion Data. *Seismol. Res. Lett.*, 90(5):1971–1986, 2019. doi: 10.1785/0220180294.

Komatitsch, D. and Tromp, J. Spectral-element simulations of global seismic wave propagation—II. Three-dimensional models, oceans, rotation and self-gravitation. *Geophys. J. Int.*, 150(1):303–318, 2002a. doi: https://doi.org/10.1046/j.1365-246X.2002.01716.x.

Komatitsch, D. and Tromp, J. Spectral-element simulations of global seismic wave propagation—II. Three-dimensional models, oceans, rotation and self-gravitation. *Geophys. J. Int.*, 150(1):303–318, 2002b. doi: https://doi.org/10.1046/j.1365-246X.2002.01716.x.

Komatitsch, D., Tromp, J., Garg, R., Gharti, H. N., Nagaso, M., Oral, E., Peter, D., Afanasiev, M., Almada, R., Ampuero, J.-P., Bachmann, E., Bai, K., Basini, P., Beller, S., Bishop, J., Bissey, F., Blitz, C., Bottero, A., Bozdag, E., Casarotti, E., Charles, J., Chen, M., Cristini, P., Durochat, C., Galvez Barron, P., Gassmoeller, R., Goeddeke, D., Grinberg, L., Gupta, A., Heien, E., Hjoerleifsdottir, V., Karakostas, F., Kientz, S., Labarta, J., Le Goff, N., Le Loher, P., Lefebvre, M., Liu, Q., Liu, Y., Luet, D., Luo, Y., Maggi, A., Magnoni, F., Martin, R., Matzen, R., McBain, G. D., McRitchie, D., Meschede, M., Messmer, P., Michea, D., Miller, D., Modrak, R., Monteiller, V., Morency, C., Nadh Somala, S., Nissen-Meyer, T., Pouget, K., Rietmann, M., Sales de Andrade, E., Savage, B., Schuberth, B., Sieminski, A., Smith, J., Strand, L., Tape, C., Valero Cano, E., Videau, B., Vilotte, J.-P., Weng, H., Xie, Z., Zhang, C.-H., and Zhu, H. SPECFEM/specfem3d: SPECFEM3D v4.1.1. doi: 10.5281/zenodo.10823181.

Krischer, L., Hutko, A. R., van Driel, M., Stähler, S., Bahavar, M., Trabant, C., and Nissen-Meyer, T. On-Demand Custom Broadband Synthetic Seismograms. *Seismol. Res. Lett.*, 88(4):1127–1140, 2017. doi: 10.1785/0220160210.

Kutschera, F., Jia, Z., Oryan, B., Wong, J. W. C., Fan, W., and Gabriel, A.-A. Rapid earthquake-tsunami modeling: The multi-event, multi-segment complexity of the 2024 Mw 7.5 Noto Peninsula Earthquake governs tsunami generation, 2024. doi: https://doi.org/10.31223/X5ZX1S. EarthArXiv.

Lotto, G. C., Jeppson, T. N., and Dunham, E. M. Fully Coupled Simulations of Megathrust Earthquakes and Tsunamis in the Japan Trench, Nankai Trough, and Cascadia Subduction Zone. *Pure App. Geophys.*, 176(9):4009–4041, 2019. doi: 10.1007/s00024-018-1990-y.

Lu, G. Y. and Wong, D. W. An adaptive inverse-distance weighting spatial interpolation technique. *Computers & Geosciences*, 34(9):1044–1055, 2008. doi: https://doi.org/10.1016/j.ca-

geo.2007.07.010.

Ma, Y. and Fu, Y. *Manifold learning theory and applications*, volume 434. CRC press Boca Raton, 2012.

Markley, F. L. Unit Quaternion from Rotation Matrix. *Journal of Guidance, Control, and Dynamics*, 31(2):440–442, 2008. doi: 10.2514/1.31730.

Melgar, D. and Bock, Y. Kinematic earthquake source inversion and tsunami runup prediction with regional geophysical data. *J. Geophys. Res. Solid Earth*, 120(5):3324–3349, 2015. doi: https://doi.org/10.1002/2014JB011832.

Minson, S. E., Simons, M., and Beck, J. L. Bayesian inversion for finite fault earthquake source models I—theory and algorithm. *Geophys. J. Int.*, 194(3):1701–1726, 2013. doi: 10.1093/gji/ggt180.

Nissen-Meyer, T., van Driel, M., Stähler, S. C., Hosseini, K., Hempel, S., Auer, L., Colombi, A., and Fournier, A. AxiSEM: broadband 3-D seismic wavefields in axisymmetric media. *Solid Earth*, 5(1):425–445, 2014. doi: 10.5194/se-5-425-2014.

Ragon, T., Sladen, A., and Simons, M. Accounting for uncertain fault geometry in earthquake source inversions – I: theory and simplified application. *Geophys. J. Int.*, 214(2):1174–1190, 2018. doi: 10.1093/gji/ggy187.

Razafindrakoto, H. N. T., Mai, P. M., Genton, M. G., Zhang, L., and Thingbaijam, K. K. S. Quantifying variability in earthquake rupture models using multidimensional scaling: application to the 2011 Tohoku earthquake. *Geophys. J. Int.*, 202(1):17–40, 2015. doi: 10.1093/gji/ggv088.

Ren, C., Yue, H., Cao, B., Zhu, Y., Wang, T., An, C., Ge, Z., and Li, Z. Rupture process of the 2020 Mw=6.9 Samos, Greece earthquake on a segmented fault system constrained from seismic, geodetic, and tsunami observations. *Tectonophysics*, 839:229497, 2022. doi: https://doi.org/10.1016/j.tecto.2022.229497.

Rodríguez-Cardozo, F., Hjörleifsdóttir, V., Jónsdóttir, K., Iglesias, A., Franco, S. I., Geirsson, H., Trujillo-Castrillón, N., and Hensch, M. The 2014–2015 complex collapse of the Bárðarbunga caldera, Iceland, revealed by seismic moment tensors. *J. Volcan. Geothermal Res.*, 416:107275, 2021. doi: https://doi.org/10.1016/j.jvolgeores.2021.107275.

Salamin, E. Application of quaternions to computation with rotations. Technical report, Stanford AI Lab, 1979.

Sambridge, M., Gallagher, K., Jackson, A., and Rickwood, P. Trans-dimensional inverse problems, model comparison and the evidence. *Geophys. J. Int.*, 167(2):528–542, 2006. doi: 10.1111/j.1365-246X.2006.03155.x.

Schultz, T. and Kindlmann, G. L. Superquadric Glyphs for Symmetric Second-Order Tensors. *IEEE Transactions on Visualization and Computer Graphics*, 16(6):1595–1604, 2010. doi: 10.1109/TVCG.2010.199.

Shi, Q., Wei, S., and Chen, M. An MCMC multiple point sources inversion scheme and its application to the 2016 Kumamoto Mw 6.2 earthquake. *Geophys. J. Int.*, 215(2):737–752, 2018. doi: 10.1093/gji/ggy302.

Shimizu, K., Yagi, Y., Okuwaki, R., and Fukahata, Y. Development of an inversion method to extract information on fault geometry from teleseismic data. *Geophys. J. Int.*, 220(2):1055–1065, 2019. doi: 10.1093/gji/ggz496.

Shimizu, K., Yagi, Y., Okuwaki, R., and Fukahata, Y. Construction of fault geometry by finite-fault inversion of teleseismic data. *Geophys. J. Int.*, 224(2):1003–1014, 2020. doi: 10.1093/gji/ggaa501.

Shoemake, K. Animating rotation with quaternion curves. *SIGGRAPH Comput. Graph.*, 19(3):245–254, 1985. doi: 10.1145/325165.325242.

Simutė, S., Steptoe, H., Cobden, L., Gokhberg, A., and Fichtner, A.

Full-waveform inversion of the Japanese Islands region. *J. Geophys. Res. Solid Earth*, 121(5):3722–3741, 2016. doi: https://doi.org/10.1002/2016JB012802.

Tape, W. and Tape, C. A geometric setting for moment tensors. *Geophys. J. Int.*, 190(1):476–498, 2012. doi: https://doi.org/10.1111/j.1365-246X.2012.05491.x.

Tinti, E., Spudich, P., and Cocco, M. Earthquake fracture energy inferred from kinematic rupture models on extended faults. *J. Geophys. Res. Solid Earth*, 110(B12), 2005. doi: https://doi.org/10.1029/2005JB003644.

Tsai, V. C., Nettles, M., Ekström, G., and Dziewonski, A. M. Multiple CMT source analysis of the 2004 Sumatra earthquake. *Geophys. Res. Lett.*, 32(17), 2005. doi: https://doi.org/10.1029/2005GL023813.

Wei, G., Chen, K., and Meng, H. Bayesian Inversion of Finite-Fault Earthquake Slip Model Using Geodetic Data, Solving for Non-Planar Fault Geometry, Variable Slip, and Data Weighting. *J. Geophys. Res. Solid Earth*, 128(2):e2022JB025225, 2023. doi: https://doi.org/10.1029/2022JB025225.

Weinstein, S. A. and Lundgren, P. R. *Finite Fault Modeling in a Tsunami Warning Center Context*, pages 451–474. Birkhäuser Basel, Basel, 2008. doi: 10.1007/978-3-7643-8757-0_2.

Worden, C. B., Thompson, E. M., Hearne, M., and Wald, D. J. ShakeMap Manual Online: Technical Manual, User's Guide, and Software Guide, 2020. doi: 10.5066/F7D21VPQ.

Yamashita, S., Yagi, Y., Okuwaki, R., Shimizu, K., Agata, R., and Fukahata, Y. Potency density tensor inversion of complex body waveforms with time-adaptive smoothing constraint. *Geophys. J. Int.*, 231(1):91–107, 2022. doi: 10.1093/gji/ggac181.

Yue, H. and Lay, T. Resolving Complicated Faulting Process Using Multi-Point-Source Representation: Iterative Inversion Algorithm Improvement and Application to Recent Complex Earthquakes. *J. Geophys. Res. Solid Earth*, 125(2):e2019JB018601, 2020. doi: https://doi.org/10.1029/2019JB018601.

Zhou, Y., Ren, C., Ghosh, A., Meng, H., Fang, L., Yue, H., Zhou, S., and Su, Y. Seismological Characterization of the 2021 Yangbi Foreshock-Mainshock Sequence, Yunnan, China: More than a Triggered Cascade. *J. Geophys. Res. Solid Earth*, 127(8):e2022JB024534, 2022. doi: https://doi.org/10.1029/2022JB024534.